Article
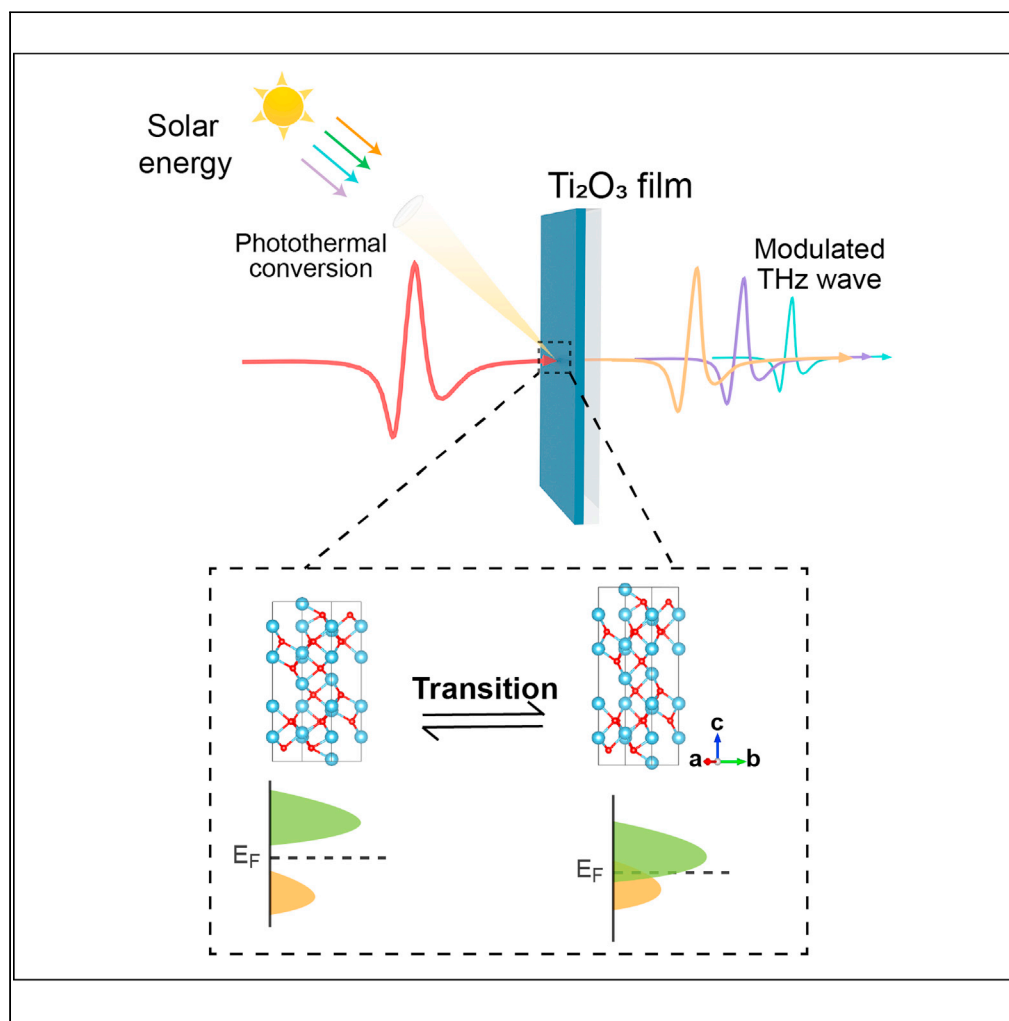
Photothermal conversion of Ti$_2$O$_3$ film for tuning terahertz waves

Yu Cai, Hongfu Zhu, Qiwu Shi, Ye Cheng, Lei Chang, Wanxia Huang

huangwanxia@scu.edu.cn

Highlights

Multilayer (TiO$_2$-Ti)$_n$ films were annealed to prepare Ti$_2$O$_3$ film

Ti$_2$O$_3$ film exhibited an excellent photothermal conversion efficiency of 90.45%

The temperature-dependent THz transmission properties with a wideband at 0.1–1 THz

THz wave could be dynamically modulated by a sunlight-controlled system

Article

Photothermal conversion of Ti$_2$O$_3$ film for tuning terahertz waves

Yu Cai,[1] Hongfu Zhu,[1] Qiwu Shi,[1] Ye Cheng,[1] Lei Chang,[1] and Wanxia Huang[1,2,*]

SUMMARY

Dynamic tuning of terahertz (THz) wave is vital for the development of next generation THz devices. Utilization of solar energy for tuning THz waves is a promising, eco-friendly, and sustainable way to expand THz application scenarios. Ti$_2$O$_3$ with an ultranarrow bandgap of 0.1eV exhibits intriguing thermal-induced metal-insulator transition (MIT), and possesses excellent photothermal conversion efficiency. Herein, Ti$_2$O$_3$ film was fabricated by a two-step magnetron sputtering method, and exhibited an excellent photothermal conversion efficiency of 90.45% and demonstrated temperature-dependent THz transmission characteristics with a wideband at 0.1–1 THz. We supposed to combine photothermal conversion characteristics with temperature-dependent THz transmission properties of Ti$_2$O$_3$ film, which could introduce solar light as the energy source for tuning THz waves. Our work will provide new sight for investigating MIT characteristics of Ti$_2$O$_3$ at THz regime and exhibit huge potential in the application of tuning terahertz waves in outdoor scenarios in the future.

INTRODUCTION

Terahertz (THz) spectral band (30–3000μm) belongs to one of the most promising regions of the electromagnetic spectrum which is located between microwave and infrared regions. In recent years, THz technologies have achieved unprecedentedly rapid development due to the outstanding optoelectronic properties of THz waves. Terahertz wave is very promising in biological detection applications because of its low invasiveness, non-destructive, and non-poisonous interaction with biological tissues (Ahmadivand et al., 2020; Smolyanskaya et al., 2018). It has also been applied in non-destructive testing due to its penetrative power through a number of highly relevant materials in industry and science (Smolyanskayaet al., 2018). Meanwhile, THz technologies are expected to meet the ever-increasing demand for high-capacity wireless communications for their much larger available bandwidth (Federici and Moeller, 2010; Koenig et al., 2013; Nagatsuma et al., 2016). What's more, terahertz spectroscopy can probe charge carrier dynamics in semiconductors, spin, and lattice oscillations in solids (Batignani et al., 2018; Cocker et al., 2021). As a result, there has been a huge demand for tunable devices at THz frequencies, as they provide tremendous opportunities for a wide range of THz applications.

To achieve the function of dynamically tuning THz waves in devices, THz waves need to be controlled, including switching, modulating, phase shifting etc (Chen et al., 2018; Manjappa et al., 2019; Zhang et al., 2015). Perovskites, two-dimensional materials and phase transition materials have been extensively used to realize these functions because of their tunable optical properties (Chen et al., 2018; Pitchappa et al., 2019; Spaldin and Ramesh, 2019). Generally, dynamic tuning of THz wave is realized by external artificial excitation sources, such as electric field, temperature, and laser (Cong et al., 2014; El Fatimy et al., 2016; Zhang et al., 2012). With the development of THz technologies, efficient utilization of solar energy to regulate THz waves is a promising tuning approach. Nevertheless, introducing solar energy as the tuning of THz waves energy source has not been reported to our knowledge.

Recently, Ti$_2$O$_3$ has attracted widespread attention in many research fields because it not only exhibits intriguing metal-insulator transition but also has an ultranarrow bandgap of 0.1eV(Huang et al., 2020; Li et al., 2019; Zeng et al., 2019). Specifically, Ti$_2$O$_3$ exhibits excellent photothermal conversion performance due to its narrow bandgap, which is capable of harvesting light across solar spectra (Wang et al., 2017). Ti$_2$O$_3$ has also exhibited high performance in mid-infrared photodetection in conjunction with graphene taking advantage of its highly efficient broadband absorption and the fast carrier transport in

graphene/Ti_2O_3 interface (Yu et al., 2018). In addition, Ti_2O_3 has attracted considerable attention because it exhibits intriguing metal-insulator transition (MIT) in the temperature range of 300–450K, which is accompanied by significant changes in optical, electric, and magnetic properties (Honig and Reed, 1968; Li et al., 2019; Nandi et al., 2020). During the transition, the changes in optical, electric and magnetic properties can be attributed to the lattice parameter alteration (Yan et al., 2012). With the variation of lattice, the crossing of bands at different points in the Brillouin zone results in the disappearance of an energy gap (Vanzandt et al., 1968). All these properties make Ti_2O_3 a promising candidate for applications in tunable optoelectronic devices. Particularly, the metal-insulator transition characteristics of Ti_2O_3 are similar to another transition metal oxide, VO_2, which has attracted great attention and exhibits advanced THz modulation properties (Liang et al., 2019; Wang et al., 2019). However, to our knowledge, the research on Ti_2O_3 in the terahertz regime has not been reported so far.

In this work, Ti_2O_3 film was fabricated on SiO_2 substrate by a two-step magnetron sputtering method. The Ti_2O_3 film exhibits excellent photothermal conversion performance with conversion efficiency of 90.45%. Besides, the THz transmission characteristics were investigated through a thermal-induced MIT of Ti_2O_3 film. Apparently, the photothermal conversion and thermal-induced MIT of Ti_2O_3 film can be related. Therefore, we supposed to combine photothermal conversion characteristics with temperature-dependent THz transmission properties of Ti_2O_3 film, which could realize sunlight-tuning THz waves. This work opens up the new concept of investigating the MIT transition of Ti_2O_3 and would meet the requirements of tuning of THz waves in outdoor scenarios in the future.

RESULTS

Fabrication and material characterizations of the Ti_2O_3 film

In our experiments, Ti_2O_3 films were prepared by a two-step magnetron sputtering method, as illustrated schematically in Figure 1A. Briefly, the $(TiO_2-Ti)_n$ films were initially obtained by magnetron sputtering, and the appropriate proportion of TiO_2 and Ti was obtained by controlling the presence or absence of oxygen in the sputtering process. Subsequently, the $(TiO_2-Ti)_n$ films were annealed to obtain the Ti_2O_3 films. To further investigate the microstructural characteristics and recognize the chemical conversion during fabrication, we examined the morphology, phase, elementary mapping, and composition of the Ti_2O_3 film (see STAR Methods).

Grazing incidence X-ray diffraction (GIXRD) was used to examine the crystalline structure and phase composition of the prepared film on SiO_2 substrate before and after annealing. Figure 1B shows the XRD patterns of TiO_2-Ti films prepared by magnetron sputtering. The film shows no detectable diffraction peaks, illustrating that the film was amorphous due to the low mobility of atoms at the low deposition temperature. As shown in Figure 1B after annealing at 1050°C for 2h, the XRD pattern of annealed film shows obvious diffraction peaks, which are indexed to Ti_2O_3 in a standard card (PDF#71-1055). No other peaks were found, which indicates that the prepared Ti_2O_3 film is of high purity and free of impurities. We also investigated the effect of proportion of TiO_2 and Ti on film composition after annealing, shown in Figure S2. The results indicated that the higher the ratio of TiO_2 to Ti, the higher the oxidation degree of the final composition of the film would be. Conversely, the lower the ratio of TiO_2 to Ti, the lower the oxidation degree of the final composition of the film would be. Moreover, the Raman spectra of as-prepared film are shown in Figure 1C. As shown in Figure 1C, for the as-prepared Ti_2O_3 film, the Raman peaks at 296.2 cm^{-1}, 338.6 cm^{-1}, and 453.3 cm^{-1}, can be assigned to the E_g modes, and the peak at 264.3 cm^{-1} and 508.3 cm^{-1}, can be assigned to the A_{1g} modes (Li et al., 2018; Wang et al., 2017). All of the observed peaks can be identified as E_g and A_{1g} modes of Ti_2O_3, indicating the high crystallization and phase purity of the Ti_2O_3 film (Li et al., 2018). X-ray photoelectron spectroscopy (XPS) measurements were carried out to elucidate the surface elemental composition and chemical states of the Ti_2O_3 film. As shown in Figure 1D, the 2p spectra of the Ti at 458.63 and 464.53 eV are the spin orbits caused by the double peaks of Ti 2p3/2 and Ti 2p1/2. The positions of the XPS peaks are consistent with those of corundum Ti_2O_3 single crystals, indicating a dominant Ti valence state of 3+ (Li et al., 2018).

The surface morphologies of Ti_2O_3 film were investigated using FESEM and the thickness of the film was examined by cross-sectional SEM. Figure 1E shows the cross-sectional SEM images of Ti_2O_3 film, with the thickness of approximately 183 nm. We also performed the thickness of film with a deposition time of 30 min before and after annealing. There is almost no change in the thickness of the film before and after annealing and the deposition rate of film is approximately 3 nm/min. As shown in Figure 1F, the surface
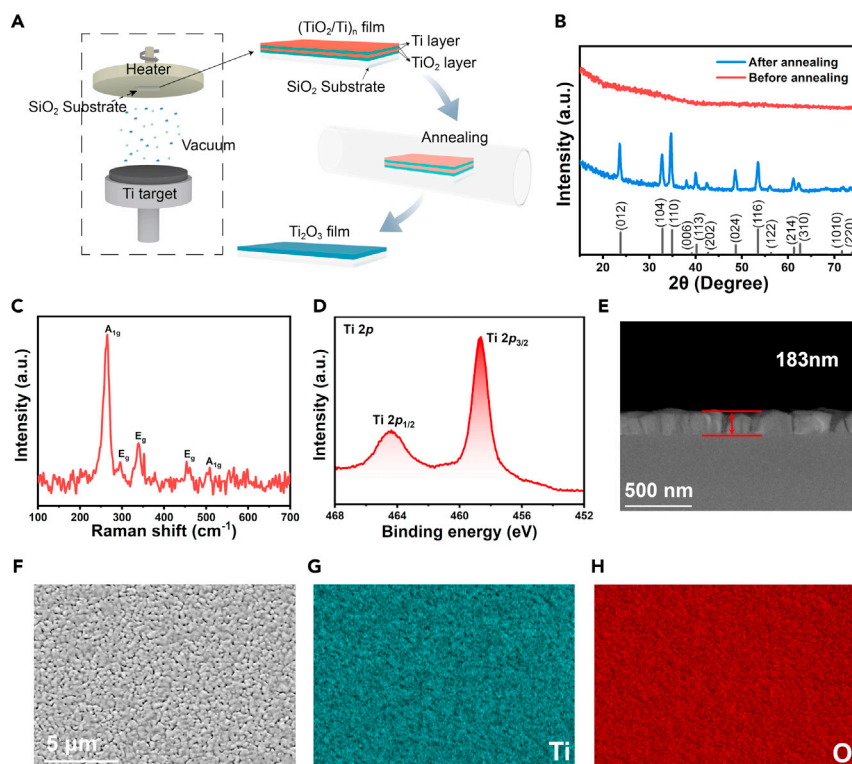
Figure 1. Fabrication and structural characterizations of the Ti$_2$O$_3$ film

(A) Schematic diagram of the fabrication processes of Ti$_2$O$_3$ film.

(B) XRD pattern of Ti$_2$O$_3$ film before and after annealing, respectively.

(C) Raman spectrum of the Ti$_2$O$_3$ film.

(D) XPS of the Ti$_2$O$_3$ film, depicting the Ti 2p peak.

(E) Cross-sectional SEM image of Ti$_2$O$_3$ film with thickness of 183 nm.

(F–H) SEM images of Ti$_2$O$_3$ film with thicknesses of 183 nm and its corresponding elemental mapping images: Ti, O, elements.

morphologies of Ti$_2$O$_3$ film are relatively compact, and the distribution of particle size is not very uniform. This difference in crystal size is possibly due to grain growth during annealing. The energy-dispersive X-ray spectroscopy (EDS) shown in Figures 1G and 1H was utilized to confirm the elemental composition of the same region in the corresponding SEM image (Figure 1F). As can be seen, the elements of Ti and O are homogeneously distributed on the surface of the film, indicating the uniformity of the composition of the film.

Photothermal conversion performance of Ti$_2$O$_3$ film

Subsequently, the photothermal conversion performance of Ti$_2$O$_3$ film was investigated. Figure 2A presents the UV-vis-NIR absorption spectra (200–2000 nm) of Ti$_2$O$_3$ film and TiO$_2$ film for contrast. As can be seen, the Ti$_2$O$_3$ film shows excellent absorption features in the region of visible and NIR spectrum, which is in contrast to TiO$_2$ which only absorbs light in the UV region. Next, we used commercial simulated sunlight (0.5 W/cm^2) as the light source, and used an infrared camera to record the surface temperature of the films under illumination to evaluate the photothermal effect performance of the Ti$_2$O$_3$ film. Upon the arrival of the equilibrium temperature of films, which was determined when the film temperature fluctuation was less than 2°C, the light was shut down and cooling process was initialized. Figure 2B shows the total temperature profile of films in response to photothermal heating and subsequently natural cooling. As can be seen, there was a sharp temperature rise of the Ti$_2$O$_3$ film as soon as the simulated solar light was turned on, which is an indicator of instantaneous heat convection within the Ti$_2$O$_3$ film. The surface temperature of Ti$_2$O$_3$ film stabilized at 95°C after 3 min of solar light illumination. By contrast, under the identical illumination condition, the surface temperature of TiO$_2$ film was heated to about 42°C. Inset in Figure 2B presents the IR photo of the Ti$_2$O$_3$ film and TiO$_2$ film after 10 min of solar light illumination. The temperature change
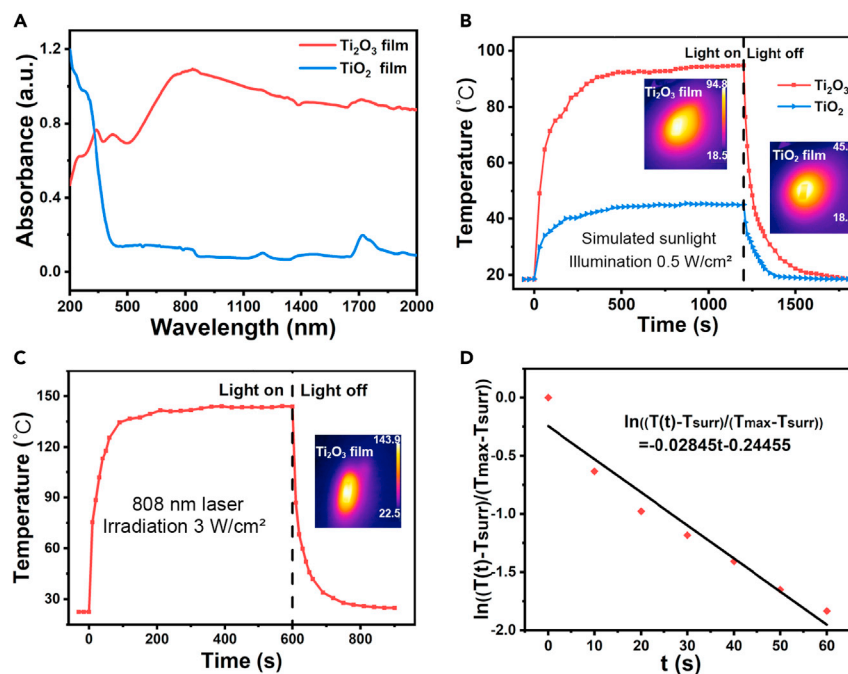
Figure 2. Photothermal conversion performance of Ti₂O₃ film

(A) UV-vis-NIR absorption spectra of Ti₂O₃ film and TiO₂ film.

(B) Surface temperatures of TiO₂ film and Ti₂O₃ film under solar illumination of 0.5 W/cm² as a function of illumination time tested by an IR camera. Inset in (B) is the IR photograph of Ti₂O₃ film and TiO₂ film under illumination from a solar simulator.

(C) The temperature relationship against time with or without 800 nm laser irradiation. Inset in (C) is the IR photograph of Ti₂O₃ film with 808 nm laser irradiation at 3 W cm⁻².

(D) Fitting plots of the temperature curve under 808 nm laser irradiation by Equation (6).

(ΔT) of TiO₂ film is about 23.5°C; however, the ΔT of Ti₂O₃ film is about 76.5°C, which is about 3.3 times more than the TiO₂ film. In our case, Ti₂O₃ film with the substantial enhancement of visible and near-infrared light absorption and the excellent photothermal performance might be attributed to the narrow-bandgap structure which enables Ti₂O₃ film to absorb the full solar spectrum (Wang et al., 2017).

To further evaluate the photothermal conversion efficiency of Ti₂O₃ film, the Ti₂O₃ film was exposed to an 808 nm laser at a power density of 3 W cm⁻² recording its temperature change. We used near-infrared 808nm laser as the light source, and used an infrared camera to record the surface temperature of the film under irradiation. As shown in Figure 2C, upon irradiation, the temperature of the surface of the Ti₂O₃ film rapidly increases due to the local heat generation on the surface by photothermal conversion. Under the laser irradiation of 3 W cm⁻², a stable surface temperature of Ti₂O₃ film at 142°C is achieved in 5 min. Inset in Figure 2C presents the IR photo of the Ti₂O₃ film after 10 min of 808 nm laser irradiation. The Ti₂O₃ film was irradiated with NIR laser for 10 min, followed by turning off the laser for cooling the film to room temperature naturally. In this case, the increased temperature (ΔT) of Ti₂O₃ film is about 121.4°C. The photothermal conversion efficiency η of Ti₂O₃ film was calculated from the thermal profile of Figure 2C via the energy balance function (Bi et al., 2020; Ren et al., 2015, 2017; Wang et al., 2017):

$$\sum_i m_i C_{p,i} \frac{\mathrm{d}T}{\mathrm{d}t} = Q_{in} - Q_{surr} \qquad \text{(Equation 1)}$$

where m and C_p are the mass and heat capacity, respectively. The suffix "i" of m and C_p refers to SiO₂ substrate and Ti₂O₃ film. T is the temperature, and t is time. Q_{in} is the photothermal energy absorbed by Ti₂O₃ film. Q_{surr} is thermal energy lost to the surroundings. Details of the calculation are given in the experimental section. According to the equation, the photothermal conversion efficiency of Ti₂O₃ film was calculated to be 90.45% under 808 nm laser irradiation.
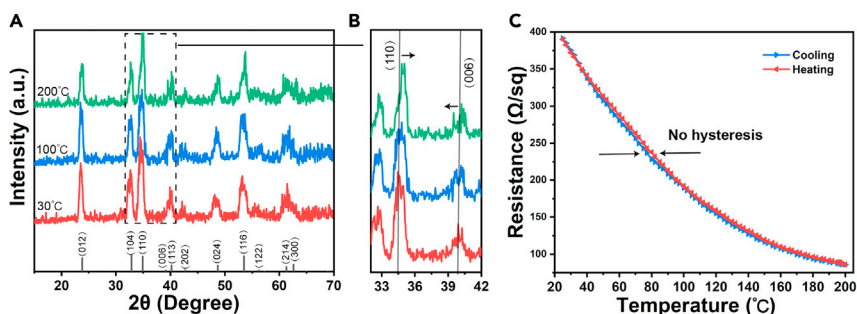
Figure 3. Thermal-induced MIT characterizations of the Ti_2O_3 film
(A and B) In-situ temperature-dependent XRD profiles of Ti_2O_3 film ranging from 30°C to 200°C and (B) magnified versions of XRD data depicted in 32°–42°.
(C) The temperature-dependent sheet resistance measured on the Ti_2O_3 film upon heating and cooling.

MIT characteristics of the Ti_2O_3 film

We carried out in-situ temperature-dependent XRD measurement under vacuum to investigate the thermal-induced MIT characteristics of the Ti_2O_3 film. Figure 3A shows the temperature-dependent XRD profiles that range from 30 to 200 K at a heating rate of 5°C/min with a holding time of 3 min at each temperature. As can be seen, the XRD profiles of Ti_2O_3 film at different temperatures are analogous, which indicates that the crystal structure of Ti_2O_3 has not changed. However, the positions of some peaks on the XRD spectrum have shifted. The shift of the diffraction peaks is not unidirectional, but it shifts on both the lower as well as higher 2θ values. Figure 3B shows the XRD profiles of (110) and (006) planes of Ti_2O_3 film at different temperatures. As can be seen, the (110) plane of Ti_2O_3 shifts to a higher diffraction angle and the (006) plane of Ti_2O_3 shifts to a lower diffraction angle with the increase of temperature. Generally, the right shift of the XRD peak position indicates the decrease of the interplanar spacing, and the corresponding left shift indicates the increase of the interplanar spacing. Meanwhile, the change of interplanar spacing is related to the lattice parameters. Ti_2O_3 has a corundum structure, and its interplanar spacing calculation equation is:

$$d_{hkl} = \frac{a}{h}\cos\alpha = \frac{b}{k}\cos\beta = \frac{c}{l}\cos\gamma \qquad \text{(Equation 2)}$$

Therefore, in our case, the peak position of (110) plane shifts to a higher diffraction angle and the peak position of (006) plane shifts to a lower diffraction angle with an increase of temperature, indicating the lattice parameter "a" decreases and the lattice parameter "c" increases, respectively. This result reveals the variation of lattice parameters during the temperature-induced MIT transition process of Ti_2O_3 film, which exhibits similar MIT transition characteristics of Ti_2O_3particles (Rice and Robinson, 1976).

Next, to investigate the thermal-induced MIT characteristics of Ti_2O_3 film, we carried out temperature-dependent square resistance measurement. Figure 3C shows the square resistance of Ti_2O_3 film against temperature from 25°C to 200°C. As can be seen, when the temperature increased from 25°C to 200°C, the square resistance of the Ti_2O_3 thin film decreased from 390.2 Ω/□ to 86 Ω/□. Alternatively, the square resistance increased from 85.9 Ω/□ to 391.4 Ω/□ with a temperature reduction from 200°C to 25°C. In this case, the temperature-dependent resistivity characteristic indicates the thermal-induced MIT of the Ti_2O_3 film, and the change of resistivity can be attributed to the change in electronic structure of Ti_2O_3 caused by temperature-induced lattice deformation (Honig, 1968; Vanzandtet al., 1968; Yoshimatsu et al., 2020). Notably, the resistance change curves during heating and cooling almost coincide, indicating that there is no hysteresis during the metal-insulator transition. Compared with VO_2, which exhibits the hysteresis loop of the square resistance against temperature (Liang et al., 2019; Zhu et al., 2020), Ti_2O_3 film is expected to achieve an extensive range of optoelectronic applications. The mid-infrared transmittance properties of the Ti_2O_3 film on SiO_2 substrate were analyzed.

THz transmission characteristics of the Ti_2O_3 film

With the behavior of temperature-dependent resistance for the Ti_2O_3 film, which would be quite suitable for application in dynamic electronic devices specially due to the sensitivity of the THz wave to the resistivity of the transmission medium, this kind of material with a dynamic change of resistivity would be available for
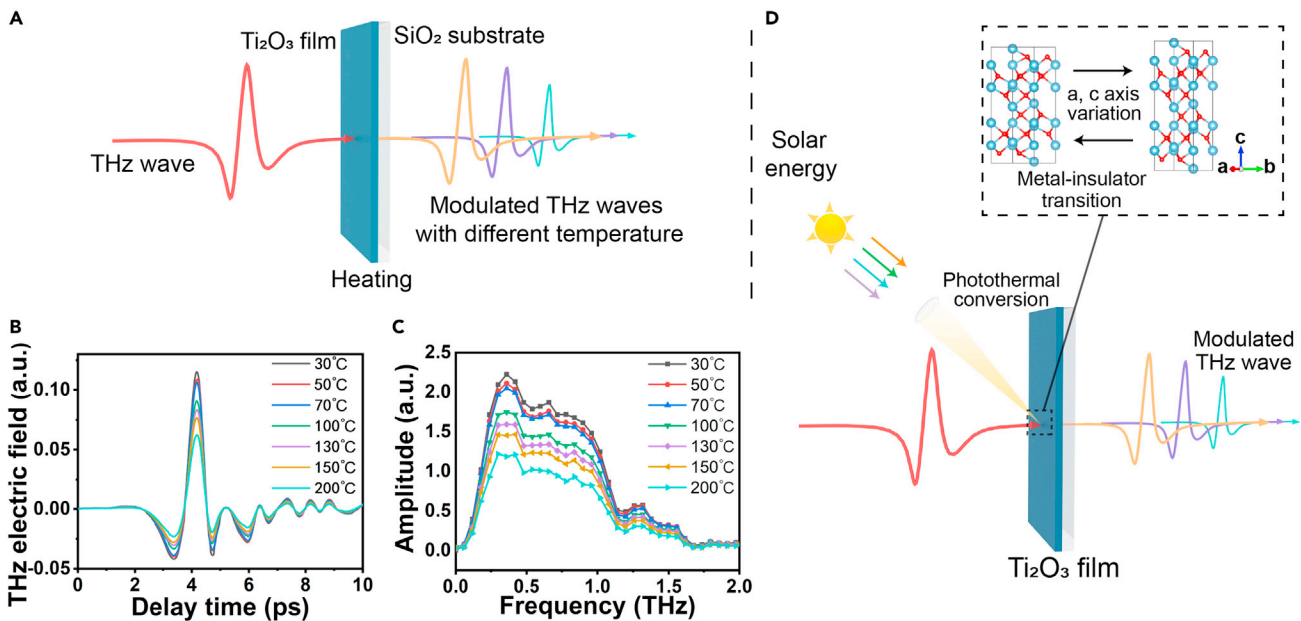
Figure 4. THz characterizations of the Ti$_2$O$_3$ film

(A) Schematic of the THz wave transmitted through the Ti$_2$O$_3$ film deposited on SiO$_2$ substrate.

(B and C) THz transmission time-domain spectra and (C) frequency-domain spectra of Ti$_2$O$_3$ film upon heating from 30°C to 200°C.

(D) Schematic illustration of tuning THz waves scenario under sunlight illumination.

the tuning of the THz transmission (Shi et al., 2016; Zhu et al., 2018). To investigate the THz transmission properties of the Ti$_2$O$_3$ film, a THz time-domain spectroscopy combined with a heating system was used to measure the THz transmission tuning properties of Ti$_2$O$_3$ film during MIT. Figure 4A shows the schematic of the THz time-domain system. The THz wave penetrates the center of the Ti$_2$O$_3$ film vertically. By heating the film to different preset temperatures under air atmosphere, the THz transmission time-domain signals were recorded and then Fourier transformed to the frequency-domain spectra. As shown in Figure 4B, the amplitude of THz transmission time-domain signals decreased gradually with increasing temperature and the transmission amplitude tuning depth can reach around 45.8%. Theoretically, the decrease in the THz transmission amplitude could be attributed to the increased absorption and reflection loss by free electrons (Mackenzie et al., 2018; Morimoto et al., 2019). In our case, the decrease in the THz transmission amplitude was caused by the increase in conductivity of Ti$_2$O$_3$ film during the MIT transition, which is consistent with the tendency of resistivity vs temperature curves in Figure 3C. Using a fast Fourier transform of the time-domain signals, we were able to obtain the THz frequency-domain spectra of the Ti$_2$O$_3$ film. As shown in Figure 4C, the THz transmission frequency-domain signals amplitude decreased monotonically with the increase of temperature. Similarly, the decrease in the THz transmission amplitude was ascribed to the decrease in resistivity of Ti$_2$O$_3$ film during the MIT transition. The signal intensity in the frequency-domain spectrum also indicated the temperature-induced MIT of Ti$_2$O$_3$ film. In addition, the tuning of THz transmission presents a wideband characteristic across the 0.1–1.1 THz range.

Naturally, considering the excellent photothermal conversion properties and temperature-dependent THz transmission characteristics of Ti$_2$O$_3$ film, we envisage combining these two features. As a prospect, let us consider a sunlight-controlled tuning of THz waves system with Ti$_2$O$_3$ film, which will expand opportunities to use THz wave scenarios in the future. As shown in Figure 4D, under the illumination of sunlight, Ti$_2$O$_3$ film could absorb solar energy to increase its temperature due to the excellent photothermal conversion performance. Subsequently, the metal-insulator transition was triggered by the variation of temperature. Finally, the tuning of THz amplitude was realized by the sunlight illumination. As for the application scenario, a sunlight-controlled THz wave switch could be utilized in outdoor. And the sunlight intensity can be adjusted through lens to control the MIT process of Ti$_2$O$_3$ film, so that THz amplitude can be modulated. Besides, due to the sensitivity of Ti$_2$O$_3$ film to light, the variation of THz amplitude also reflects the change of light intensity. By collecting changes in terahertz signals, the corresponding devices can be controlled to respond to changes in ambient light intensity. This kind of utilizing solar energy to modulate THz waves

amplitude requires no external energy sources, which could save energy or be utilized in emergencies. This kind of tuning THz waves method would expand the application range of terahertz technologies, and exploit a novel route toward achieving dynamic tuning of THz waves.

Conclusions

In summary, we demonstrated a two-step magnetron sputtering method for the fabrication of Ti_2O_3 film, investigated its photothermal conversion performance, and then demonstrated the THz transmission properties of Ti_2O_3 film across this MIT transition. The fabricated Ti_2O_3 film exhibited an excellent photothermal conversion efficiency of 90.45%. Moreover, the Ti_2O_3 film can achieve a THz tuning depth of nearly 45.8% with a wideband at 0.1–1THz owing to the change in conductivity of Ti_2O_3 film during the MIT transition. Therefore, based on the excellent photothermal conversion properties and temperature-dependent THz transmission characteristics of Ti_2O_3 film, we envisage applying the high-performance photothermal conversion characteristics to tuning of THz waves, which could realize solar light-tuning THz waves. Our work not only discloses the thermal-induced MIT transition of Ti_2O_3 through THz transmission characteristics but also opens a venue for expansion of THz application scenarios.

Limitations of the study

In this paper, Ti_2O_3 polycrystalline film was fabricated on SiO_2 substrate by a two-step magnetron sputtering method. We have demonstrated the application potential of Ti_2O_3 film in the field of sunlight-tuning THz waves. Therefore, the performance of the Ti_2O_3 film on devices needed to be evaluated. Compared with polycrystalline film, epitaxial films with highly ordered atomic arrangement demonstrate unusual optical or electrical properties. Further work needs to be done to investigate the performance of Ti_2O_3 epitaxial film. Besides, the deposition process for the high-quality epitaxial films and the performance optimization of Ti_2O_3 film will be the direction of our continued research.

STAR★METHODS

Detailed methods are provided in the online version of this paper and include the following:

- KEY RESOURCES TABLE
- RESOURCE AVAILABILITY
  - Lead contact
  - Materials availability
  - Data and code availability
- METHOD DETAILS
  - Fabrication of film
  - Material characterizations
  - Calculation of the photothermal conversion efficiency

SUPPLEMENTAL INFORMATION

Supplemental information can be found online at https://doi.org/10.1016/j.isci.2021.103661.

AUTHOR CONTRIBUTIONS

Y.C. conceived the study and wrote the manuscript. H.Z. carried out the THz transmission experiments. W.H. supervised the project. All authors made a substantial contribution to the discussion of the content and reviewed the manuscript before submission.

REFERENCES

Ahmadivand, A., Gerislioglu, B., Ahuja, R., and Mishra, Y.K. (2020). Terahertz plasmonics: the rise of toroidalmetadevices towards immunobiosensings. Mater. Today *32*, 108–130. https://doi.org/10.1016/j.mattod.2019.08.002.

Batignani, G., Fumero, G., Kandada, A.R.S., Cerullo, G., Gandini, M., Ferrante, C., Petrozza, A., and Scopigno, T. (2018). Probing femtosecond lattice displacement upon photo-carrier generation in lead halide perovskite. Nat. Commun. *9*, 1971. https://doi.org/10.1038/s41467-018-04367-6.

Bi, D.G., Li, Y.Y., Yao, Y.B., Tao, T., Liang, B., and Lu, S.G. (2020). Preparation and characterizations of flexible photothermalTi2O3-PVAnanocomposites. J. Alloys Compounds *825*, 153998. https://doi.org/10.1016/j.jallcom.2020.153998.

Chen, Z., Chen, X., Tao, L., Chen, K., Long, M., Liu, X., Yan, K., Stantchev, R.I., Pickwell-MacPherson, E., and Xu, J.-B. (2018). Graphene controlled Brewster angle device for ultra broadband terahertz modulation. Nat. Commun. *9*, 4909. https://doi.org/10.1038/s41467-018-07367-8.

Cocker, T.L., Jelic, V., Hillenbrand, R., and Hegmann, F.A. (2021). Nanoscale terahertz scanning probe microscopy. Nat. Photon. *15*, 558–569. https://doi.org/10.1038/s41566-021-00835-6.

Cong, L., Xu, N., Gu, J., Singh, R., Han, J., and Zhang, W. (2014). Highly flexible broadband terahertz metamaterial quarter-wave plate. Laser Photon. Rev. *8*, 626–632. https://doi.org/10.1002/lpor.201300205.

El Fatimy, A., Myers-Ward, R.L., Boyd, A.K., Daniels, K.M., Gaskill, D.K., and Barbara, P. (2016). Epitaxial graphene quantum dots for high-performance terahertz bolometers. Nat. Nanotechnol. *11*, 335. https://doi.org/10.1038/nnano.2015.303.

Federici, J., and Moeller, L. (2010). Review of terahertz and subterahertz wireless communications. J. Appl. Phys. *107*, 111101. https://doi.org/10.1063/1.3386413.

Honig, J.M. (1968). Nature of electrical transition in Ti2O3. Rev. Mod. Phys. *40*, 748. https://doi.org/10.1103/RevModPhys.40.748.

Honig, J.M., and Reed, T.B. (1968). Electrical properties OF Tl2O3 single crystals. Phys. Rev. *174*, 1020. https://doi.org/10.1103/PhysRev.174.1020.

Huang, H., Wang, C., Li, Q., Wang, R., Yang, Y., Muhetaer, A., Huang, F., Han, B., and Xu, D. (2020). Efficient and full-spectrum photothermaldehydrogenation of ammonia borane for low-temperature release of hydrogen. Adv. Funct. Mater. 2007591. https://doi.org/10.1002/adfm.202007591.

Koenig, S., Lopez-Diaz, D., Antes, J., Boes, F., Henneberger, R., Leuther, A., Tessmann, A., Schmogrow, R., Hillerkuss, D., Palmer, R., et al. (2013). Wireless sub-THz communication system with high data rate. Nat. Photon. *7*, 977–981. https://doi.org/10.1038/nphoton.2013.275.

Li, Y., Weng, Y., Zhang, J., Ding, J., Zhu, Y., Wang, Q., Yang, Y., Cheng, Y., Zhang, Q., Li, P., et al. (2018). Observation of superconductivity in structure-selected Ti2O3 thin films. Npg Asia Mater. *10*. https://doi.org/10.1038/s41427-018-0050-5.

Li, Y., Yu, Z.G., Wang, L., Weng, Y., Tang, C.S., Yin, X., Han, K., Wu, H., Yu, X., Wong, L.M., et al. (2019). Electronic-reconstruction-enhanced hydrogen evolution catalysis in oxide polymorphs. Nat. Commun. *10*, 3149. https://doi.org/10.1038/s41467-019-11124-w.

Liang, W., Jiang, Y., Guo, J., Li, N., Qiu, W., Yang, H., Ji, Y., and Luo, S.-N. (2019). Van der Waals heteroepitaxialVO2/mica films with extremely low optical trigger threshold and large THz field modulation depth. Adv. Opt. Mater. *7*, 1900647. https://doi.org/10.1002/adom.201900647.

Mackenzie, D.M.A., Whelan, P.R., Boggild, P., Jepsen, P.U., Redo-Sanchez, A., Etayo, D., Fabricius, N., and Petersen, D.H. (2018). Quality assessment of terahertz time-domain spectroscopy transmission and reflection modes for graphene conductivity mapping. Opt. Express *26*, 9220–9229. https://doi.org/10.1364/oe.26.009220.

Manjappa, M., Solanki, A., Kumar, A., Sum, T.C., and Singh, R. (2019). Solution-processed lead iodide for ultrafast all-optical switching of terahertz photonic devices. Adv. Mater. *31*, 1901455. https://doi.org/10.1002/adma.201901455.

Morimoto, T., Nagai, M., Minowa, Y., Ashida, M., Yokotani, Y., Okuyama, Y., and Kani, Y. (2019). Microscopic ion migration in solid electrolytes revealed by terahertz time-domain spectroscopy. Nat. Commun. *10*, 2662. https://doi.org/10.1038/s41467-019-10501-9.

Nagatsuma, T., Ducournau, G., and Renaud, C.C. (2016). Advances in terahertz communications accelerated by photonics. Nat. Photon. *10*, 371–379. https://doi.org/10.1038/nphoton.2016.65.

Nandi, S., Tripathi, R., Das Adhikary, G., Kumar, P., and Misra, A. (2020). Ultrahigh infrared photoresponse in titanium sesquioxide at mott-insulator transition. Adv. Mater. Inter. 2001091. https://doi.org/10.1002/admi.202001091.

Pitchappa, P., Kumar, A., Prakash, S., Jani, H., Venkatesan, T., and Singh, R. (2019). Chalcogenide phase change material for active terahertz photonics. Adv. Mater. *31*, 1808157. https://doi.org/10.1002/adma.201808157.

Ren, H., Tang, M., Guan, B., Wang, K., Yang, J., Wang, F., Wang, M., Shan, J., Chen, Z., Wei, D., et al. (2017). Hierarchical graphenefoam for efficient omnidirectional solar-thermal energy conversion. Adv. Mater. *29*, 1702590. https://doi.org/10.1002/adma.201702590.

Ren, W.Z., Yan, Y., Zeng, L.Y., Shi, Z.Z., Gong, A., Schaaf, P., Wang, D., Zhao, J.S., Zou, B.B., Yu, H.S., et al. (2015). A near infrared light triggered hydrogenated black TiO2 for cancer photothermaltherapy. Adv. Healthc. Mater. *4*, 1526–1536. https://doi.org/10.1002/adhm.201500273.

Rice, C.E., and Robinson, W.R. (1976). Structural-changes associated with semiconductor-to-metal transition IN Tl2O3. Mater. Res. Bull. *11*, 1355–1359. https://doi.org/10.1016/0025-5408(76)90045-3.

Shi, Q., Chai, G., Huang, W., Shi, Y., Huang, B., Wei, D., Qi, J., Su, F., Xu, W., and Lu, T. (2016). Fabrication of nanocrystalline lambda-Ti3O5 with tunable terahertz wave transmission properties across a temperature induced phase transition. J. Mater. Chem. C *4*, 10279–10285. https://doi.org/10.1039/c6tc03108k.

Smolyanskaya, O.A., Chernomyrdin, N.V., Konovko, A.A., Zaytsev, K.I., Ozheredov, I.A., Cherkasova, O.P., Nazarov, M.M., Guillet, J.P., Kozlov, S.A., Kistenev, Y.V., et al. (2018). Terahertz biophotonics as a tool for studies of dielectric and spectral properties of biological tissues and liquids. Prog.Quan.Electron. *62*, 1–77. https://doi.org/10.1016/j.pquantelec.2018.10.001.

Spaldin, N.A., and Ramesh, R. (2019). Advances in magnetoelectricmultiferroics. Nat. Mater. *18*, 203–212. https://doi.org/10.1038/s41563-018-0275-2.

Vanzandt, L.L., Honig, J.M., and Goodenou, J.B. (1968). Resistivity and magnetic order IN Tl2O3. J. Appl. Phys. *39*, 594. https://doi.org/10.1063/1.2163536.

Wang, J., Li, Y.Y., Deng, L., Wei, N.N., Weng, Y.K., Dong, S., Qi, D.P., Qiu, J., Chen, X.D., and Wu, T. (2017). High-performance photothermal conversion of narrow-bandgapTi2O3 nanoparticles. Adv. Mater. *29*, 1603730. https://doi.org/10.1002/adma.201603730.

Wang, R.-k., Wang, H., An, Z.-q., He, J.-s., Zhang, C.-l., Pan, G.-p., and Li, X. (2019). Two-step hydrothermal growth of a thin film of vanadium dioxide on sapphire with large terahertz modulation depth. J. Appl. Phys. *125*, 163104. https://doi.org/10.1063/1.5050640.

Yan, W.W., Fang, M., Liu, M., Kang, S.H., Wang, R.N., Zhang, L.D., and Liu, L. (2012). Semiconductor-metal transition of titanium sesquioxidenanopowder. J. Appl. Phys. *111*, 123509. https://doi.org/10.1063/1.4729801.

Yoshimatsu, K., Hasegawa, N., Nambu, Y., Ishii, Y., Wakabayashi, Y., and Kumigashira, H. (2020). Metallic ground states of undopedTi$_2$O$_3$ films induced by elongated c-axis lattice constant. Sci. Rep. *10*, 22109. https://doi.org/10.1038/s41598-020-79182-5.

Yu, X.C., Li, Y.Y., Hu, X.N., Zhangg, D.L., Tao, Y., Liu, Z.X., He, Y.M., Haque, M.A., Liu, Z., Wu, T., and Wang, Q.J. (2018). Narrow bandgap oxide nanoparticles coupled with graphene for high performance mid-infrared photodetection. Nat. Commun. *9*, 4299. https://doi.org/10.1038/s41467-018-06776-z.

Zeng, P., Chen, M.F., Jiang, S.X., Li, Y.F., Xie, X., Liu, H., Hu, X.Y., Wu, C., Shu, H.B., and Wang, X.Y. (2019). Architecture and performance of the novel sulfur host material based on Ti$_2$O$_3$microspheres for lithium-sulfur batteries. ACS Appl. Mater. Inter. *11*, 22439–22448. https://doi.org/10.1021/acsami.9b05874.

Zhang, S., Zhou, J., Park, Y.-S., Rho, J., Singh, R., Nam, S., Azad, A.K., Chen, H.-T., Yin, X., Taylor, A.J., and Zhang, X. (2012). Photoinduced handedness switching in terahertz chiral metamolecules. Nat. Commun. *3*, 942. https://doi.org/10.1038/ncomms1908.

Zhang, Y., Qiao, S., Lang, S., Wu, Z., Yang, Z., Feng, Z., Sun, H., Zhou, Y., Sun, L., Chen, Z., et al. (2015). Gbps terahertz external modulator based on a composite metamaterial with a double-channel heterostructure. Nano Lett. *15*, 3501–3506. https://doi.org/10.1021/acs.nanolett.5b00869.

Zhu, H.-F., Du, L.-H., Li, J., Shi, Q.-W., Peng, B., Li, Z.-R., Huang, W.-X., and Zhu, L.-G. (2018). Near-perfect terahertz wave amplitude modulation enabled by impedance matching in VO2 thin films. Appl. Phys. Lett. *112*, 081103. https://doi.org/10.1063/1.5020930.

Zhu, H.F., Li, J., Du, L.H., Huang, W.X., Liu, J.B., Zhou, J.H., Chen, Y.F., Das, S., Shi, Q.W., Zhu, L.G., and Liu, C.L. (2020). A phase transition oxide/graphene interface for incident-angle-agile, ultrabroadband, and deep THz modulation. Adv. Mater. Inter. 2001297. https://doi.org/10.1002/admi.202001297.

STAR★METHODS

KEY RESOURCES TABLE

REAGENT or RESOURCE	SOURCE	IDENTIFIER
Chemicals, peptides, and recombinant proteins		
Ti Target (99.995%)	ZhongNuo Advanced Material Technology Co.,Ltd	http://www.znxc.com/
SiO$_2$ single crystal substrates (110)	HeFei Crystal Technical Material Co.,Ltd	http://www.ctmwafer.com/
Argon (Ar) (99.999%)	Sichuan Qiaoyuan Gas Co.,Ltd	CAS: 7440-37-1
Oxygen (O$_2$) (99.99%)	Sichuan Qiaoyuan Gas Co.,Ltd	CAS: 7782-44-7
Ethanol	Chengdu Chron Chemicals Co.,Ltd	CAS: 64-17-5
Other		
GIXRD, Rigaku D Max 2500 Pc Powder X Ray Diffractometer	Rigaku	https://www.rigaku.com/products/xrd/smartlab
XPS, Thermo Scientific K-Alpha Surface Analysis	Thermal Fisher Scientific	https://www.thermofisher.cn/cn/zh/home.html?cid=ebz_bus_sbu_r04_cn_0se_bdk_bz_pur_gene_aBrand_pc_hp_051021_title
UV-Visible Spectrophotometer, Shimadzu UV-3600i Plus	Shimadzu	https://www.shimadzu.com.cn/an/spectro/uv/uv-3600iplus/index.html

RESOURCE AVAILABILITY

Lead contact

Further information and requests for resources and materials should be directed to the lead contact, Wan-xia Huang (huangwanxia@scu.edu.cn).

Materials availability

This study did not generate new unique reagents.

Data and code availability

- All data reported in this paper will be shared by the lead contact upon request.

- This paper does not report original code.

- Any additional information required to reanalyze the data reported in this paper is available from the lead contact upon request.

METHOD DETAILS

Fabrication of film

The preparation processes of Ti$_2$O$_3$ film were divided into two main stages: firstly, the (TiO$_2$-Ti)$_n$ films were fabricated by magnetron sputtering, and then the prepared films were annealed to obtain the Ti$_2$O$_3$ films. Specifically, as schematically illustrated in Figure 1A, the (TiO$_2$-Ti)$_n$ films were deposited by magnetron sputtering, in which the argon plasma was used to systematically bombard a titanium target (purity = 99.995%) in the presence or absence of oxygen to form the TiO$_2$ and Ti layer respectively. In the magnetron sputtering process, in every five-minute, the oxygen presence and oxygen absence time were 210 and 90 seconds respectively. Single crystal SiO$_2$(001) sheets were used as substrates, which were cleaned by son-ication in acetone, ethanol and deionized(DI) water in sequence for 30 minutes each, and dried in an oven at 80°C for 30 min. After loading the substrates into the sputtering chamber, the distance between the target and substrates was set as 10 cm, and then the chamber was heated to 100°C to remove residual water and evacuated to a base pressure of below 8 × 10^{-4} Pa. A flow of 200 *sccm* Ar was used to keep the deposition pressure maintained at 0.30 Pa. The target material was presputtered for 5 minutes before deposition to remove surface oxides and contaminants. Thereafter, the TiO$_2$-Ti films were placed in a molybdenum

boat and annealed at 1050°C in argon (purity of 99.999%) at a flow rate of 400 *sccm* for 2 h and cooled down to room temperature naturally to obtain the Ti_2O_3 film.

Material characterizations

Grazing incidence X-ray diffraction(GIXRD) patterns were recorded using a Rigaku D/Max-2500/PC setup with a Cu Kα (0.15418 nm) radiation. In-situ temperature-dependent XRD profiles of films were measured with a BrukerD8 Advance diffractometer, using CuKa radiation. Raman measurements were carried out with a confocal micro-Raman system (Horiba Aramis/ JobinYvonHR800) at ambient conditions, using a solid state laser (excitation wavelength is 532 nm). X-ray photoelectron spectroscopy (XPS) analysis was also performed to characterize the electronic structure and Ti-O hybridization on the Ti_2O_3 films' surfaces. Scanning electron microscopy (SEM) images and corresponding element mapping/EDS spectrum were obtained on a field-emission microscope (Inspect F50, FEI Company). UV-vis-NIR absorption spectra were collected by UV-3600 plus Shimadzu UV-vis-NIR spectrophotometer at room temperature. The resistance variation of the films with temperature was investigated by using the four-point probe method. The THz transmission characteristics of the transparent Ti_2O_3 film were measured by the terahertz time-domain spectroscopy (THz-TDS) system.

Calculation of the photothermal conversion efficiency

The photo-thermal conversion efficiency η of Ti_2O_3 film was calculated via the energy balance function(Bi et al., 2020; Ren et al., 2015, 2017; Wang et al., 2017):

$$\sum_i m_i C_{p,i} \frac{dT}{dt} = Q_{in} - Q_{surr} \qquad \text{(Equation 3)}$$

where m and C_p are the mass and heat capacity, respectively. The suffix "i" of m and C_p refers to SiO_2 substrate and Ti_2O_3 film. T is the temperature, and t is time. Q_{in} is the photothermal energy absorbed by Ti_2O_3 film:

$$Q_{in} = I - A_\lambda - \eta \qquad \text{(Equation 4)}$$

Where I is the laser power, A_λ is the absorbance of Ti_2O_3 film at the wavelength of 808 nm, and η is the photothermal conversion efficiency of Ti_2O_3 film. Q_{surr} is thermal energy lost to the surroundings:

$$Q_{surr} = hs\Delta T \qquad \text{(Equation 5)}$$

Where h is the heat transfer coefficient, s is the cross-sectional area perpendicular to thermal conduction, and ΔT is the changed temperature, which is referred to $T\text{-}T_{surr}$.

When the temperature is stabilized, $\frac{dT}{dt} = 0$, so the equation can be:

$$Q_{in} = Q_{surr} = hs(T_{max} - T_{surr}) \qquad \text{(Equation 6)}$$

The temperature vs. time after removal of the incident light is given by eq:

$$T(t) = T_{surr} + (T_{max} - T_{surr})exp(-Bt) \qquad \text{(Equation 7)}$$

where T_{max} and T_{surr} are the Ti_2O_3 film temperature and ambient temperature of the surrounding, and $B = \frac{hs}{\sum_i m_i C_{p,i}}$.

B can be acquired from fitting the heating curve data after removal of the incident laser in Figure 2C. As shown in Figure 2D, the value of B was found to be 0.02845. Mass of Ti_2O_3 film was 1.6×10^{-4}g. C_p of Ti_2O_3 was 0.786J g^{-1} K^{-1}. Mass of SiO_2 substrate was 0.22g. C_p of SiO_2 substrate was 0.745J g^{-1} K^{-1}. So we can get hs equals 4.663 mW/K.

According to the Equations (2), (4), and (6), the photothermal conversion efficiency η can be expressed as following:

$$\eta = \frac{hs(T_{max} - T_{surr})}{I \cdot A_\lambda} \qquad \text{(Equation 8)}$$

where $(T_{max} - T_{surr})$ was 121.4 K. I was 588.75 mW where the diameter of light spot was 0.5 cm. A_λ was 1.081. Thus the photo-thermal conversion efficiency of Ti_2O_3 film was calculated to be 90.45% under 808 nm laser irradiation.